




# Velocity map imaging and cross sections of $\text{Fe}(\text{CO})_5$ for FEBIP applications

Maria Pinte<sup>1,a</sup> , Nigel Mason<sup>1,2,b</sup>, and Maria Tudorovskaya<sup>3</sup>

<sup>1</sup> Department of Molecular Processing, School of Physical Sciences, Kent University, Canterbury CT2 7HZ, UK

<sup>2</sup> School of Physical Sciences, The Open University, Milton Keynes MK7 6AA, UK

<sup>3</sup> Quantemol Ltd, London, UK

Received 14 March 2022 / Accepted 4 August 2022 / Published online 12 September 2022

© The Author(s) 2022

**Abstract.** The present paper intends to be a new study of a widely used precursor in nanostructure deposition and FEBID processes with focus on its fragmentation at collisions with low energy electrons. Newer developments in nanotechnology with applications to focused electron beam-induced deposition (FEBID) and extreme ultraviolet lithography (EUVL) based on irradiation-induced chemistry come with advances in the size of the nanostructures at the surface and their flexibility in creating highly complex 3D structures. The deformation in the main structures of the FEBID process characterized by elongation, reduction in diameter of the main structure and the deposition of additional thin layers around the structure, on the substrate, are results of the secondary electrons effect, colliding with energies lower than 20 eV.  $\text{Fe}(\text{CO})_5$  is one of the most used compounds in FEBID processes as it has a high vaporization pressure and has been shown to provide high-purity deposits (over 90%). This paper combines experiment and simulations to study electron scattering from  $\text{Fe}(\text{CO})_5$ , using Quantemol-N simulations with mass spectroscopy techniques to present the fragmentation pathways and channel distributions for each of the resulting negative ions at low electron energies, while experimental data on dissociative electron attachment make use of the velocity-sliced map imaging (VMI) technique to determine the anions at the incident electron energies. The Quantemol-N simulation package as a standalone is used to study collision processes of low-energy electrons with  $\text{Fe}(\text{CO})_5$  molecules including elastic, electronic excitation, and dissociative electron attachment (DEA) cross sections for a wide range of process in nuclear industry, medical research and quantum chemistry.

## 1 Introduction

### 1.1 Focused electron beam-induced dissociation

Focused electron beam-induced deposition (FEBID) [1] is an emerging technique that can be used for nano-size structure growth [2] as one of the newest methods to write nm-level structures, nanorods, nanowires (for tips used in deposition, in mask repair), and in the development of nanomaterials such as superconductors, magnetic materials, multilayer structures, metamaterials [3, 4]. Still in the initial phase, the method attracts a lot of the industry research on nanolithography. The feed stock gases used in FEBID are metallic compounds containing organic parts such as oxides, carbonyls and halogens. Such gases are dissociated by high energy electrons to produce metallic deposits reaching current deposits purity rates in Fe of > 95% [5], Fe > 80% [3] and Pt purity > 99% [6] as the highest ones achieved.

However, in the FEBID process, backscattered and secondary electrons are produced at low energies that subsequently interact with the target molecules close to 0 eV. At such low energies, the dominant process leading to the molecules dissociation is dissociative electron attachment (DEA).

As part of a larger project, ELENA, and a continuation of a chain of projects involved with the study of focused electron beam-induced deposition (FEBID) [7] and dissociative electron attachment (DEA) [9, 10], the present study provides a detailed analysis of  $\text{Fe}(\text{CO})_5$  using velocity-sliced map imaging (VMI) whilst also using the Quantemol-N code to generate a set of low energy cross sections. Up to now, no VMI data have been declared on  $\text{Fe}(\text{CO})_5$  compound, though mass spectrum measurements have been taken and data can be found on DEA to  $\text{Fe}(\text{CO})_5$  clusters [11], irradiation of  $\text{Fe}(\text{CO})_5$  in electron-stimulated studies [12],  $\text{Fe}(\text{CO})_5$  deposited on Argon nanoparticles, ligand exchange dynamics of  $\text{Fe}(\text{CO})_5$  in solutions [15],  $\text{Fe}(\text{CO})_5$  bond acceptor–donator reactions [13], dynamics studies of  $\text{Fe}(\text{CO})_5$  by transient ionization and dissociation after ligand stabilization of  $\text{Fe}(\text{CO})_5$  aggregates [14, 15].

<sup>a</sup> e-mail: [mp675@kent.ac.uk](mailto:mp675@kent.ac.uk) (corresponding author)

<sup>b</sup> e-mail: [n.j.mason@kent.ac.uk](mailto:n.j.mason@kent.ac.uk)

The velocity-sliced map imaging (VMI) method uses a time-of-flight spectrometer for mass selection of the ions produced from the interaction of a molecular beam with an electron beam created by an electron gun equipped with a tungsten filament. The product ions are directed towards an MCP detector and a phosphor screen where a 2D image is captured by the use of a CCD camera. Used to study the dynamics of dissociative ionization and dissociative electron attachment of molecules such as CO, H<sub>2</sub>O, NH<sub>3</sub>, CH<sub>4</sub>, H<sub>2</sub>S, H<sub>2</sub>D<sub>2</sub>, N<sub>2</sub>O, CF<sub>4</sub>, C<sub>2</sub>H<sub>2</sub>, the VMI method gives accurate information on angular distribution and kinetic energies of these two processes; however, to date, the method has not been largely used for metal-containing compounds for nanotechnology applications.

This paper is organized as follows: firstly, we discuss the properties of the molecule (molecular geometry, vibrational frequencies and electron affinities) according to the fragmentation channels, followed by the experimental set-up and the experimental results, while in the last section, we present the computational details and Quantemol-N computational results.

## 1.2 Molecular target

Capable of providing iron nanostructures with high purity and exhibiting high ferromagnetic behavior, Fe(CO)<sub>5</sub> is a good candidate for the creation of structures at the nanoscale for magnetic sensing elements, hard disc data storage, logic devices, and sensors. Extensive studies on the applicability of Fe-carbonyls to nanosize structure growth by focused electron beam-induced deposition have been carried out, summarized in the work of De Teresa and Pacheco [1] and van Dorp and Hagen [2]. Complete SCF field simulations of Fe(CO)<sub>5</sub> using Quantemol-N offer reliable output cross sections of the molecule induced collisions with excited electrons. The geometry of the molecule is presented in Fig. 1. The molecule is a symmetric dihedral (D<sub>3h</sub> point work group) with the Fe atom in the center. The Cartesian coordinates used in this work are listed in Table 5 (Appendix II). Table 4 further summarizes the vibrational frequencies corresponding to the specific fragmentation channels, as well as the electron affinities.

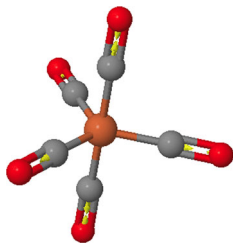
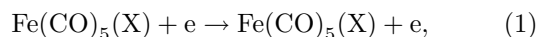


**Fig. 1** Fe(CO)<sub>5</sub> geometry. Orange: Fe atom. Grey: C atoms. Red: O atoms

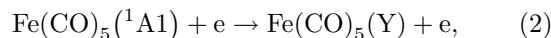
## 1.3 Electron impact processes

In this paper, we seek to provide the electron impact cross sections for a variety of collision processes including elastic scattering:



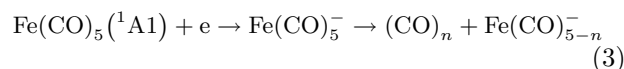
where X is the ground state of the molecule.

Electron-impact excitation:



where Y stands for an excited state different from the ground state and.

Dissociative electron attachment:



The latter process goes through formation of a resonance, i.e., an incoming electron forming a short-living quasi-bound state with the target molecule. This intermediate resonance then decays into fragments, therefore, the index  $n = (1 \dots 5)$ .

The probability of a scattering process is described with the use of scattering cross section. Such cross sections may be computed with the help of the R-matrix theory [16]. The idea of the method lies in separating the scattering space into an inner and outer region. The inner region, separated from the outer region by a sphere of a certain radius, must contain the molecule with its N electrons and the incoming electron, which becomes indistinguishable from the molecular orbitals. The outer region only contains the incoming electron, which interacts with the potential of the N-electron molecule. The Schrödinger equation is solved separately for the target molecule, in the inner region, and in the outer region, and the solutions are matched at the boundary.

For (1) and (2), the cross section can be derived unambiguously if the wave function of the system is known. In the close-coupling (CC) expansion used in this paper, the wave function in the inner region is presented in terms of N-electron target states,  $\Phi_i^N(x_1 \dots x_N)$ , continuum orbitals  $u_{ij}(x_{N+1})$ ,  $a_{ijk}$  and  $b_{ij}$  magnitude coefficients, quadratically integral functions  $\Psi_i^{N+1}$  constructed from target occupied and virtual orbitals:

$$\Psi_k^{N+1} = A \sum_{ij} a_{ijk} \Phi_i^N(x_1 \dots x_N) u_{ij}(x_{N+1}) + \sum_i b_{ij} \Psi_i^{N+1} \quad (4)$$

In the calculation, some electrons are “frozen” in the “frozen” orbitals (22, 10, 11, 2), whilst the remaining electrons as well as the scattered electrons can be redistributed between remaining bound orbitals, and the scattered electron occupies the continuum orbitals.

For (3), additional data are needed. The R-matrix routines are used to find the energy,  $E$ , and the width,  $\Gamma$ , of the quasi-bound states, or resonances, when the incoming electron is temporarily bound to the molecule. It is assumed that the cross section of scattering via an individual resonance behaves as described by Breit and Wigner:

$$\sigma_{BW}(E, r) = 2\pi \frac{\Gamma^2/4}{(E - V_r(r))^2 - \Gamma^2/4}, \quad (5)$$

where  $r$  is the distance between the dissociating fragments and  $V_r$  is the effective resonance potential. It is then assumed that this intermediate state dissociates into fragments effectively behaving like a diatomic molecule. A dissociative electron attachment estimator is incorporated in the Quantemol-N. The model is based on a few assumptions:

- Relative to the active bond length(s), the molecular target potential can be approximated as Morse potential; the negative ion potential is either Morse potential or an exponentially decaying function. This allows vibrational wave functions corresponding to perturbing the bond between the dissociating fragments to be determined.
- The potentials can be described with the vibrational frequency corresponding to the ground vibrational state and the dissociation energy of the molecular target.
- The cross section has a Breit–Wigner shape; each resonance formed during the scattering process is characterized by its position and width.

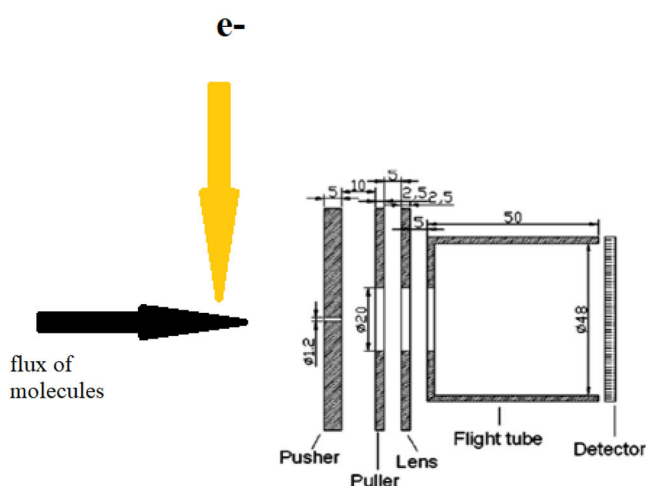
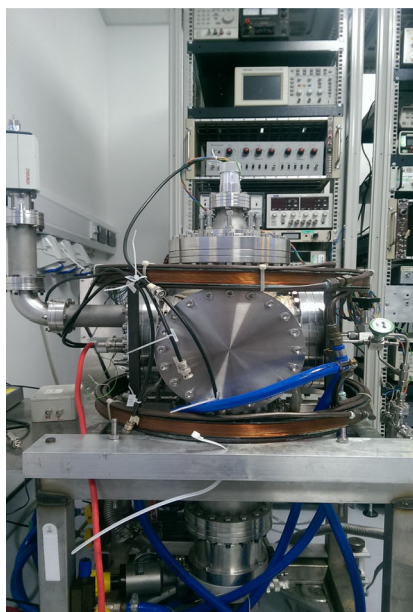


**Fig. 2** Velocity-sliced map imaging apparatus at University of Kent, consisting of the high vacuum chamber, electron gun, and Helmholtz coils

More detailed description can be found in the paper of Munro et al. [16].

## 2 Experiment

### 2.1 Experimental setup

The VMI apparatus is presented in Fig. 2. The vacuum system is maintained at a pressure of  $\sim 10^{-9}$  mbar by a system of pumps, consisting of a turbopump together with a backing pump, an oil-free Varian TriScroll high-speed scroll pump and a set of ion and Pirani gauges. The gas line is served by Oerlikon Leybold 30 l/s turbo pump at a pressure of  $10^{-3}$  mbar. The electrons involved in the electron-molecule collision processes are produced by thermionic emission from the 0.2 mm tungsten filament in the electron gun and collimated at 90 deg to the flux of molecules with both electrostatic lenses and a magnetic field generated by two Helmholtz coils. The molecular beam is introduced to the chamber through the gas line, and it is perpendicular to the electron beam. The measurement system consists of a flight tube, a MCP detector, a phosphor screen and a CCD camera.

The CLUSTER apparatus in Bratislava is presented in greater detail in reference [30].

### 2.2 Experimental results and discussion

In the DEA process, the  $\text{Fe}(\text{CO})_5$  undergoes dissociation into five negative ions, process characterized by full fragmentation as a result of the loss of the five CO ligands. The negative ion mass spectrum with the yields

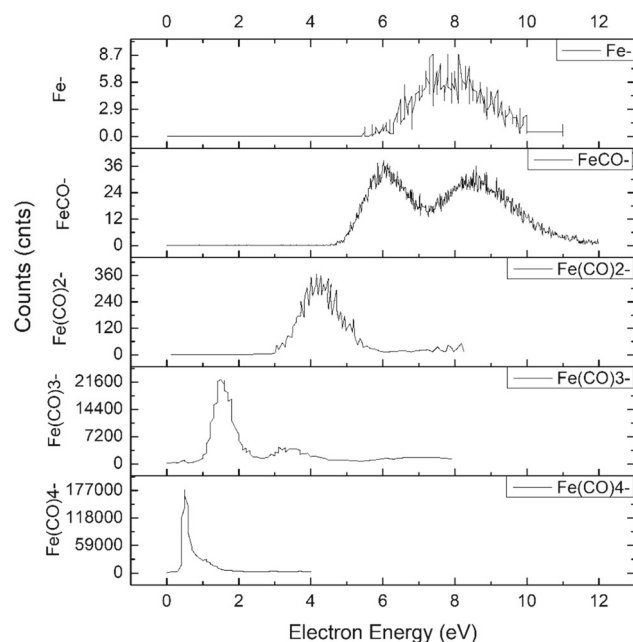


**Fig. 3** Yields to electron energy spectrum of  $\text{Fe}(\text{CO})_5$

to energy curves of each of the resonances is presented in Fig. 3 and summarized in Table 1. The spectrum, in good agreement with the data reported from our TOF VMI (Time-of-Flight velocity-sliced map imaging) and with the initial work of Allan et al. [17] and Lengyel et al. [18], presents a number of five peaks corresponding to five anions.

Two possible fragmentation pathways in the collision or ionization processes of  $\text{Fe}(\text{CO})_5$  can take place according to [17, 18], as consecutive [18] and simultaneous ligand breakage [17], with higher focus given to simultaneous dissociation in the present work:

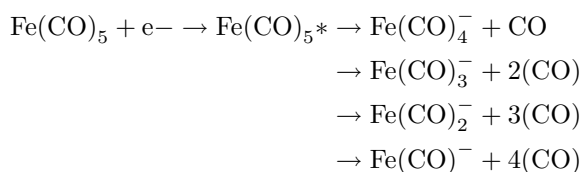
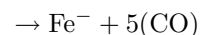


**Table 1** Experimental peak parameters and attributed channels

Attributed channel	Peak position, eV	Peak height, ion counts	Peak width, eV
$\text{Fe}(\text{CO})_5 + e^- \rightarrow \text{Fe}(\text{CO})_5^* \rightarrow \text{Fe}(\text{CO})_4^- + \text{CO}$	0.2/0.6/1.2	1738	1.49
$\text{Fe}(\text{CO})_5 + e^- \rightarrow \text{Fe}(\text{CO})_5^* \rightarrow \text{Fe}(\text{CO})_3^- + 2\text{CO}$	1.3; 3.4	212; 32	1.6; 1.79
$\text{Fe}(\text{CO})_5 + e^- \rightarrow \text{Fe}(\text{CO})_5^* \rightarrow \text{Fe}(\text{CO})_2^- + 3\text{CO}$	4.2	35	3.18
$\text{Fe}(\text{CO})_5 + e^- \rightarrow \text{Fe}(\text{CO})_5^* \rightarrow \text{Fe}(\text{CO})^- + 4\text{CO}$	5.8; 8.3	1500; 1500	3.9; 5.35
$\text{Fe}(\text{CO})_5 + e^- \rightarrow \text{Fe}(\text{CO})_5^* \rightarrow \text{Fe}^- + 5\text{CO}$	8	8	4.4



The electrons accelerated by the ground, extractor and repeller, using the magnetic field created by the pair of Helmholtz coils, cross a molecular beam collimated at 90 deg to the electron beam creating ions negatively charged that pass a flight tube reaching a detector at different positions on the Chevron pattern of the detector and being further projected on a phosphor screen supporting a CCD camera that acquires images of the inner 3D 100 ns thin slice of the anions Newton sphere in a set of 2D images. The acquired images are processed, denoised and averaged, using Python programming language with Scikit, Pandas and OpenCV packages. The denoised pictures of  $\text{Fe}(\text{CO})_4^-$  (a),  $\text{Fe}(\text{CO})_3^-$  (b),  $\text{Fe}^-$  (c) are presented in Fig. 4.

The most predominant ion produced by DEA,  $\text{Fe}(\text{CO})_4^-$ , shows a resonance peaking around 0.2 eV. Allan et al. [17] in their experimental work positioned their  $\text{Fe}(\text{CO})_4^-$  resonance peak at a value of 0.08 eV, defined by a narrow width of 70 meV and a second cleavage of the same resonance with lower amplitude at 0.26 eV, fragmentation induced by an electron beam with a resolution of 100 meV. The high count rates in the dissociation peaks of the resonances near 0 eV show that the dominant process at these energies is intramolecular vibration causing the breakage of the ligand and a high rise in the dissociation cross sections. The loss of one ligand in the DEA process at energies close to 0 eV is considered a transition process of the  $\text{Fe}(\text{CO})_5$  in the neutral ground state  $\sigma$  to  $\pi^*$  excited state, losing one of the axial CO bonds to metal to form  $\text{Fe}(\text{CO})_4^-$ .

The experimental data from the VMI position these peaks at two higher energies, 0.2 eV and 0.6 eV. At 0.2 eV, the anion presents a peak with high yields,  $\sim 100,000$  cnts, followed by an increase in the number of anions with the maximum of the resonance at 0.6 eV ( $\sim 50,000$  cnts) and a smaller shoulder at 1.2 eV. A transition from  $\sigma$  to  $\pi^*$  of the  $\text{Fe}(\text{CO})_5$  parent in ground state with  $C_{4v}$  geometry to  $\text{Fe}(\text{CO})_5^*$  in  $C_{2v}$  geometry occurs, followed by dissociation in two fragments, a negatively charged  $\text{Fe}(\text{CO})_4^-$  in  $C_{2v}$  geometry and the CO neutral fragment.

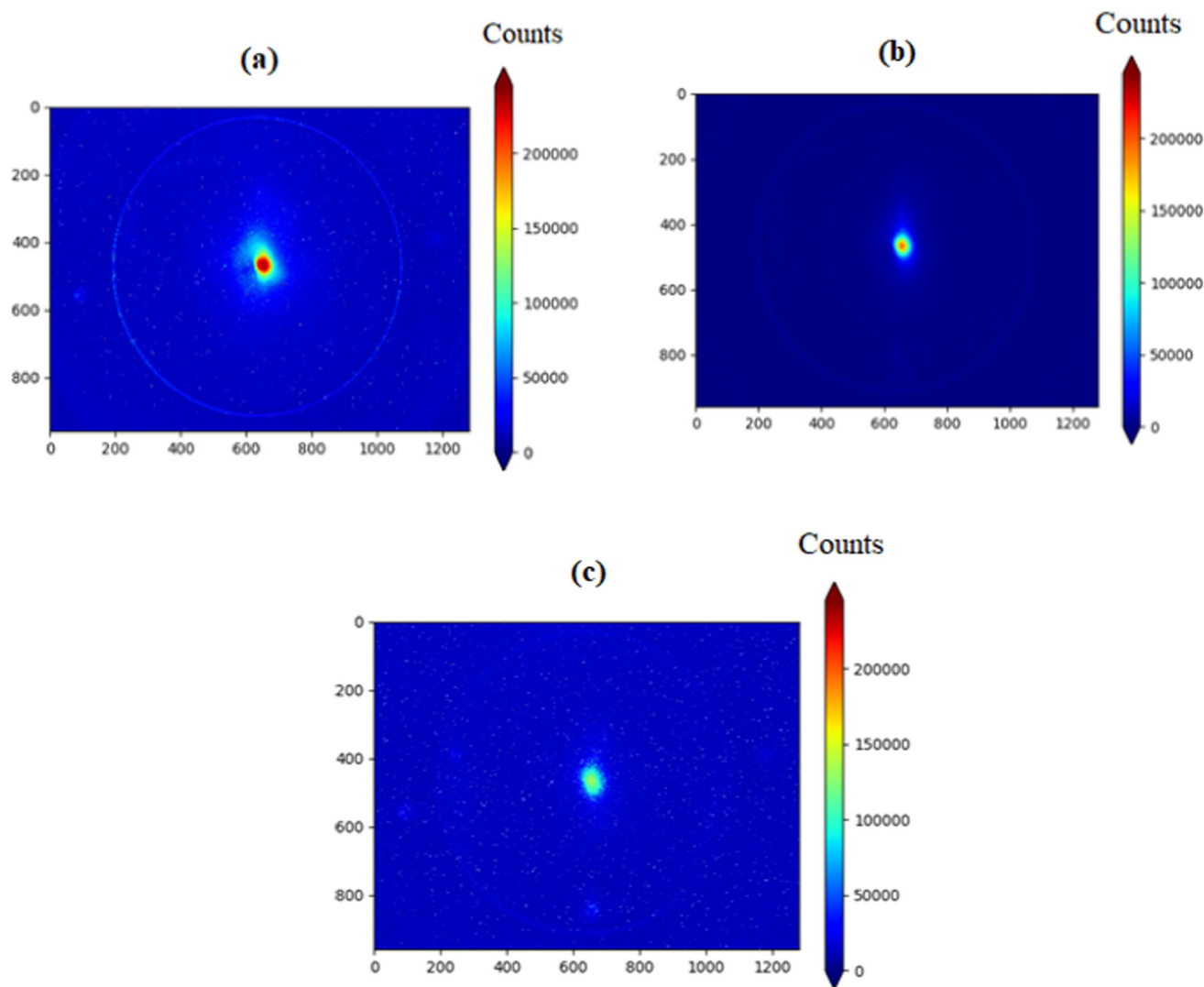


**Fig. 4**  $\text{Fe}(\text{CO})_5$  anions imaged ( $840 \times 1200$  pixels) by VMI CCD camera with colorbar representing the number of collected anions:  $\text{Fe}(\text{CO})_4^-$  **a**,  $\text{Fe}(\text{CO})^-$  **b**,  $\text{Fe}^-$  **c**

Differences in the position of the maximum of the  $\text{Fe}(\text{CO})_3^-$  resonance come in the work of Lacko et al. 2018 and Lengyel et al. 2017 with values of 1.2 eV [18] and 1.4 eV [17], while a less counts peak of the resonance falls at 3.6 eV [18] and 3.8 eV [17] compared to our VMI work where the two peaks of the resonance were found at 1.3 eV and 3.4 eV, with average differences in the range of 0.1–0.2 eV. Similar differences are observed for the rest of the anions. The  $\text{Fe}(\text{CO})_2^-$  has an average difference of  $\sim 0.1$  eV in the highest peak of the resonance found at 4.2 eV [17] and 4.3 eV [18]. The second peak of the resonance is found at 8.9 eV in all cited sources, and there is good agreement between [17, 18] and VMI data in the position of the  $\text{FeCO}^-$  incident electron energies found at 5.9 eV and 8.5 eV.

The lightest anion  $\text{Fe}^-$  from our VMI work is higher in energy by 1 eV compared to the work of Lengyel et al. 2017.

The electron affinity of the ions determined experimentally by Engelking and Lineberger [19] by using an electrical discharge ion source and a Wien filter with an Ar ion laser (Table 4, Appendix 1) is comparable with the work of Shuman et al. [11]. They report a value of the Fe affinity of  $0.164 \pm 0.02$  eV, higher than presented in the work of Chen et al. [20], exhibiting a value of 0.153 eV, determined experimentally by slow electron velocity map imaging (SEVI) method, as to be the only one out of the five ions to be reported. The thermochemistry data from Shuman et al. [11] fall back to the measurements of Engelking and Lineberger [19] with changes to the uncertainty corrections. They employed variable electron and neutral density attachment spectroscopy (VENDAMS) technique and flowing afterglow Langmuir probe mass spectrometer (FALP) to determine the accurate values of electron affinity and bond dissociation energies for the negative ions formed in the DEA process of  $\text{Fe}(\text{CO})_5$ .

The bond dissociation energies and electron affinities of anions presented by Engelking and Lineberger [19] are lower in values than the ones reported by Shuman et al. [11] by almost 1 eV, ranging from  $0.2 \pm 0.4$  eV to  $1.4 \pm 0.3$  eV for the  $\text{Fe}(\text{CO})_2^-$  ion, not reporting any BDE for the lightest anion  $\text{Fe}^-$ . The work of Chen et al. [20] focuses on calculating only the lightest anion bond dissociation energy with a value of 0.153 eV. The electron affinities have opposite behavior with values under 1 eV in the work of Shuman et al. [11] with a value of  $0.151 \pm 0.003$  eV for the lightest anion and reaching  $2.4 \pm 0.3$  eV for  $\text{Fe}(\text{CO})_4^-$ , while Engelking and Lineberger report values between  $1.22 \pm 0.02$  eV and  $2.4 \pm 0.3$  eV (Annex 1 Table 4). The values we used for our maximum kinetic energies calculations are based on the values reported by Shuman et al. [11] and Chen et al. [20].

The maximum values of the kinetic energies [21] have been calculated using the excess energy  $E_e = EA - \text{BDE} + E_i$ , where EA is the electron affinity of the anion, BDE is the bond dissociation energy and  $E_i$  is the incident electron energy. The maximum kinetic energy for the  $\text{Fe}(\text{CO})_4^-$  fragment is determined using the electron affinity of the fragment from Shuman et al. [11] of  $2.4 \pm 0.3$  eV, a bond dissociation energy of 1.81 eV and the electron incident energy of 0.2 eV, with a resultant value of 0.61 eV. The kinetic energy of  $\text{Fe}(\text{CO})_4^-$  from the VMI measurement is presented in Fig. 5. Accordingly, the recorded data show a high rise slope between 0.2 and 1 eV, with the two maximum points in amplitude at 0.2 eV and 0.85 eV.

$\text{Fe}(\text{CO})_3^-$  has a higher electron affinity in the work of Shuman et al. [11], with a value of  $1.915 \pm 0.085$  eV compared to  $1.22 \pm 0.02$  eV reported by Engelking and Lineberger [19], with the maximum kinetic energy presenting high discrepancy between the two cited works, of approximately 0.8 eV. The kinetic energy of  $\text{Fe}(\text{CO})_3^-$  from velocity map imaging is a distribution of energies ranging from 0 eV to 0.9 eV and peaking at 0.6 eV. The fragmentation channel corresponding to  $\text{Fe}(\text{CO})_3^-$  anion presents a peak at 1.3 eV with the width of the resonance of 1.1 eV, and another smaller resonance peak at 3.4 eV, both very narrow compared to lighter anions. Engelking and Lineberger [19] present the appearance of a so-called hot band at the transition from  $\text{Fe}(\text{CO})_3^-$  to  $\text{Fe}(\text{CO})_2^-$  in the dissociation process, though the fragmentation energy of 2 eV does not agree well with the VMI data reported here or the quadrupole mass spectra reported by Lacko et al. [21] and cluster data from Lengyel et al. [22].

The  $\text{FeCO}^-$  is found at 8.5 eV. There is a  $\sim 1$  eV discrepancy between the work of Shuman et al. [11], with an electron affinity value of  $1.157 \pm 0.005$  eV, and Engelking and Lineberger [19] with a value of  $2.4 \pm 0.3$  eV, giving a kinetic energy of  $8.197 \pm 0.005$  eV in the first case and  $9.44 \pm 0.3$  eV, in the second case. Engelking and Lineberger [19] present the  $\text{FeCO}_2^-$  as having lower electron affinity compared to  $\text{FeCO}^-$ , but showing similar features. The VMI data are in good agreement with the work of Shuman et al. [11], with kinetic energy values ranging between  $3.87 \pm 0.02$  eV

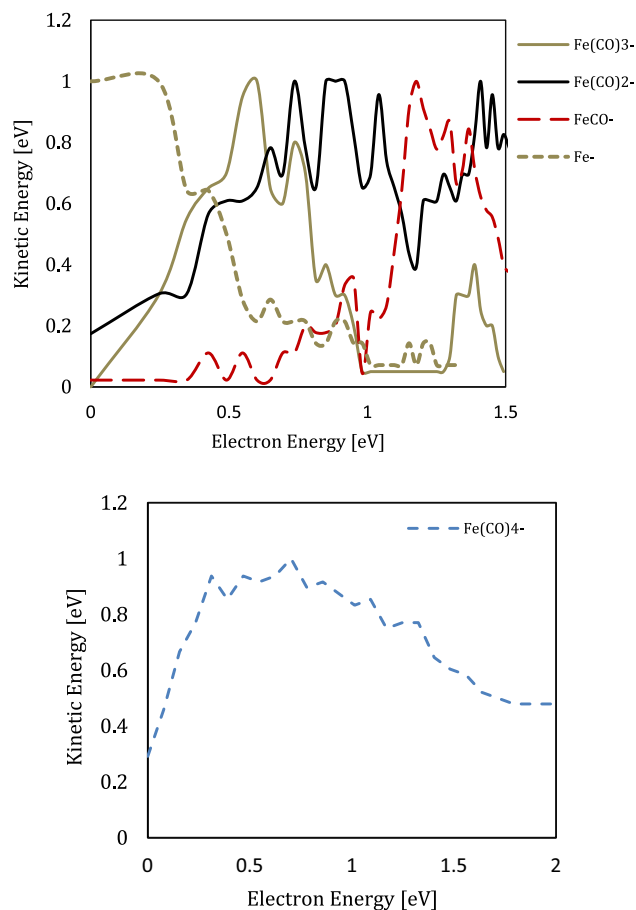


**Fig. 5** Kinetic energies of the negative ions

and  $4.27 \pm 0.02$  eV, and electron affinities of  $1.8 \pm 0.02$  eV and  $1.22 \pm 0.02$  eV.

Higher electron affinity is observed in the transition from  $\text{FeCO}$  to  $\text{Fe}$ , assigned to the bond strength of the CO, though the work of Engelking and Lineberger [19] explains this by a stabilization of d orbitals of  $\pi$  symmetry in the interaction with the CO  $\pi^*$  orbitals and a destabilization of d orbitals with  $\nu$  symmetry by the  $\nu$  orbitals of CO. The  $\text{Fe}^-$  ion is presented in a separate work by Chen et al. [20], who used a VMI method to determine the electron affinity by means of bombarding with  $\text{Ar}^+$  atoms. The calculated kinetic energy release maximum for the  $\text{Fe}^-$  ion is  $9.998 \pm 0.003$  eV.

Angular distributions of the anions (Fig. 6) were calculated from the VMI images. The  $\text{Fe}(\text{CO})_2^-$  presents high symmetry, with lower amplitude from 80 deg up to 90 deg with backwards cross sections. The same behavior can be seen for  $\text{Fe}(\text{CO})_3^-$  and  $\text{Fe}(\text{CO})_4^-$  fragments with higher amplitudes close to 90 deg. The  $\text{Fe}^-$  is rather symmetric, compared to the higher mass fragments. The higher mass anions  $\text{Fe}(\text{CO})_4^-$  to  $\text{Fe}(\text{CO})_3^-$  present a  $C_{2v}$  symmetry, while the symmetry of the lightest anions changes to  $C_{3v}$ . All anions are symmetric to 95 deg line. A widening of the angular distribution is observed for  $\text{Fe}(\text{CO})_3^-$  that we assign to its instability and short lived life compared to the rest of the anions.

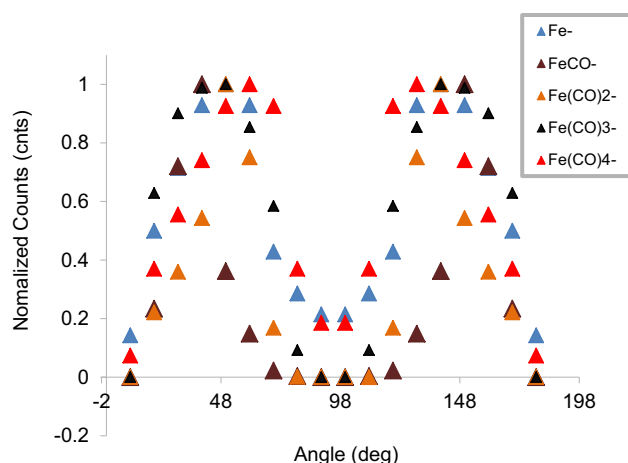


**Fig. 6** The angular distribution data of the negatively charged fragments, recorded with our VMI, as well as our kinetic energies show no triplet state dissociation, with the appearance of only one ring at the investigated channels

### 3 Simulations

#### 3.1 Numerical setup

The VMI experimental results presented in Sect. 2 are complemented with scattering calculations carried out with Quantemol-N software which makes use of the UKRmol code suite [16, 23, 24]. UKRmol computes scattering cross sections based on the R-matrix theory. In the R-matrix theory, the time-independent Schrödinger equation is solved for the system molecule + incoming electron. The incoming electron is treated as indistinguishable from the target electrons inside of a sphere which is big enough to include the molecule and its orbitals. Outside of the sphere, the scattered electron is treated separately and the solution is energy-dependent.

The true symmetry point group of  $\text{Fe}(\text{CO})_5$  is  $D_{3h}$ . The input symmetry point group allowed by Quantemol-N in the calculation is  $C_{2v}$ ; therefore, all the orbitals and excited states found in the calculation are irreducible representations of this group, namely  $[A_1, B_1, B_2, A_2]$ . We use the cc-pVDZ basis set to find both the ground and excited states of the molecular target, and for the scattering calculations, and the configuration interaction quantum chemistry model is employed. The ground state energy is  $-1824.94$  Hartree (1 Hartree \approx 27.211 eV), and the configuration is  $23(a_1)^2, 11(b_1)^2, 11(b_2)^2, 3(a_2)^2$  which is consistent with the result obtained by Daniel et al. [25]. For comparison, the NIST database gives ground state energy in the range  $-1825.77$  to  $-1830.75$  Ha depending on the basis set. The highest occupied molecular orbital has  $b_1$  symmetry and energy  $-7.59$  eV.

Scattering calculations are performed with the close coupling model; the R-matrix sphere radius is 13 Bohr. The convergence of the model was tested by increasing

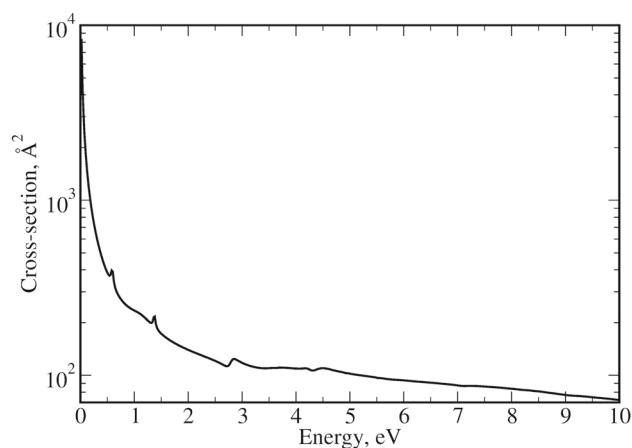


**Fig. 7** Electron elastic scattering cross section for  $\text{Fe}(\text{CO})_5$

the complete active space (CAS) and running the calculations with different basis sets. The frozen orbitals are  $22(a_1)^2, 10(b_1)^2, 11(b_2)^2, 2(a_2)^2$  and the complete active space used in the calculation is  $25(a_1)^2, 11(b_1)^2, 12(b_2)^2, 4(a_2)^2$ . Therefore, there are 3 open orbitals and 4 virtual orbitals included in the calculation.

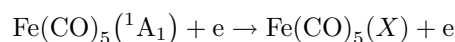
Note that the R-matrix method is less accurate at the energy above the ionization threshold. However, the calculated ionization energy is 7.59 eV which is in good agreement with Norwood et al. [26].

### 4 Elastic electron and electron-impact excitation cross sections

The calculation shows that the ground state is  $^1A_1$  in the  $C_{2v}$  point group or  $^1A_1'$  in the  $D_{3h}$  point group.

Figure 7 shows the elastic scattering cross section for the electron energy in the range 0–10 eV.

The electronic excitation of the  $^1A_1$  state is characterized by the following processes:

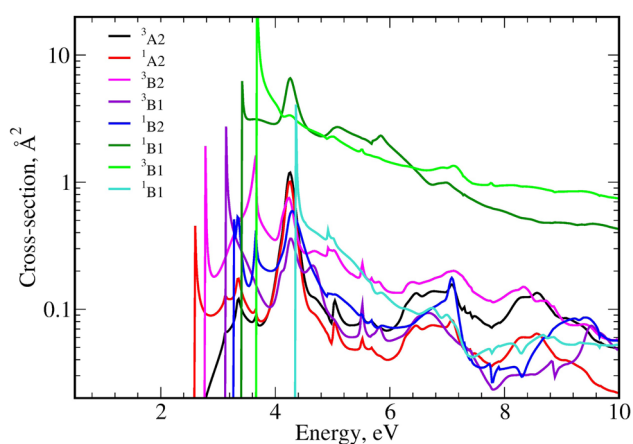


where  $X$  stands for an excited state. Energies, symmetry, and multiplicity of the first 8 excited states are given in Table 2.

Figure 8 shows excitation cross sections from the ground state to the excited states listed in Table 2. For the metal carbonyl only three allowed transitions can be seen:  $^1A_1' \rightarrow ^1,^3E'$ ,  $^1A_1' \rightarrow ^1,^3E''$  and  $^1A_1' \rightarrow b^1E'$  [27]. Rubner et al. [27] present the appearance of the  $\text{Fe}(\text{CO})_4$  and  $\text{Fe}(\text{CO})_3$  fragments in the frequency range of  $^1,^3E'$  (corresponding to  $1,3A_2, 1,3B_1$  and  $1,3B_2$  in our calculations), and the appearance of  $\text{Fe}(\text{CO})_4, \text{Fe}(\text{CO})_3$  and  $\text{Fe}(\text{CO})_2$  as a  $b^1E'$  (corresponding to  $1,3B_{1,2}$  in our calculations). The work of Rubner et al. [27] used three separate models comparing the excitation bands for each of the states: CASSCF, MR-CCI, and ACPF. For our work, only  $d \rightarrow \pi_{\text{CO}}^*$  transitions states were

**Table 2** Multiplicity and symmetry of the excited states in  $C_{2v}$  and corresponding excitation energies

Excited state	Excitation energy, eV
$^3A_2$	2.58
$^1A_2$	2.77
$^3B_2$	3.13
$^3B_1$	3.27
$^1B_2$	3.40
$^1B_1$	3.67
$^3B_1$	4.35
$^1B_1$	4.51

**Fig. 8** Electronic excitation of  $Fe(CO)_5$  by electron impact from the ground state. The curves are labeled correspondingly to the excited state multiplicity and symmetry

taken into account as the only states involved in the metal-CO ligand dissociation.

The excitation cross sections presented from our calculations are in good agreement with the data from

Rubner et al. [27]. It can be seen that the  $^1A_1'$  excitation singlet falls in the same energy range as the dissociation excitations  $\sim 4$  eV for  $Fe(CO)_5$  with the appearance of  $Fe(CO)_4^-$ ,  $Fe(CO)_3^-$  and  $Fe(CO)_2^-$ .

## 5 Dissociative electron attachment cross sections

Dissociative electron attachment is assumed to go via the intermediate resonance  $Fe(CO)_5^-$ . We have separated the energy range to a few sub-ranges of interest corresponding to different fragmentation channels. For each fragmentation channel, a specific set of parameters has to be used. Table 3 outlines the parameters used in the calculations.

In order to associate each channel with a vibrational frequency, the exact character of the modes has to be taken into account. The vibrational modes can be visualized on ChemTube3D [7]. We make an assumption that bending modes do not participate in the dissociation; if certain modes lead to simultaneous stretching of Fe-CO bonds, then these bonds will break in the DEA process.

In the dissociation process, the  $Fe(CO)_5$  molecule undergoes fast ionization from a  $v$  state to  $\pi^*$  state,  $Fe(CO)_5^-$ , followed by a further detachment of an electron, characterized by a thermal process Allan et al. [17], or loss of one CO ligand. Allan et al. [17] reports the dissociation of the  $Fe(CO)_5^-$  into  $Fe(CO)_4^- + CO$  as plausible at two peak energies, 0.08 eV and 0.25 eV electron energy. From the mass spectrum (Bratislava work on experimental CLUSTER apparatus) and [18], the peaks corresponding to this fragmentation channel are at 0.08 eV and 0.26 eV. From our VMI experiments, we found the fragmentation channel leading to the formation of  $Fe(CO)_4^-$  at 0.2 eV incident energy, close to the data reported by them with a bond dissociation energy of 1.81 eV.

The CO-stretch excitation cross section was found at 0.66 eV that might correspond to the 0.2 eV  $Fe(CO)_4^-$

**Table 3** Dissociative electron attachment parameters for each fragmentation channel. Electron affinity and bond breaking energies are from [11]

DEA fragmentation channel	Energy range, eV	Vibrational frequency, $cm^{-1}$ , mode	Electron affinity, eV	Bond dissociation energy, eV
$Fe(CO)_5 + e^- \rightarrow Fe(CO)_4^- + CO$	0–1	2093.4 ( $E'$ )	$2.4 \pm 0.3$	1.81
$Fe(CO)_5 + e^- \rightarrow Fe(CO)_3^- + 2(CO)$	1–2.5	2118.85 ( $A_1'$ )	$1.915 \pm 0.085$	1.84
$Fe(CO)_5 + e^- \rightarrow Fe(CO)_2^- + 3(CO)$	2.5–6	2093.4 ( $E'$ )	$1.22 \pm 0.02$	1.55
$Fe(CO)_5 + e^- \rightarrow Fe(CO)^- + 4(CO)$	4–10	2120.24 ( $A_2''$ )	$1.157 \pm 0.005$	1.46
$Fe(CO)_5 + e^- \rightarrow Fe^- + 4(CO)$	6–10	2192.65 ( $A_1'$ )	$0.151 \pm 0.003$	



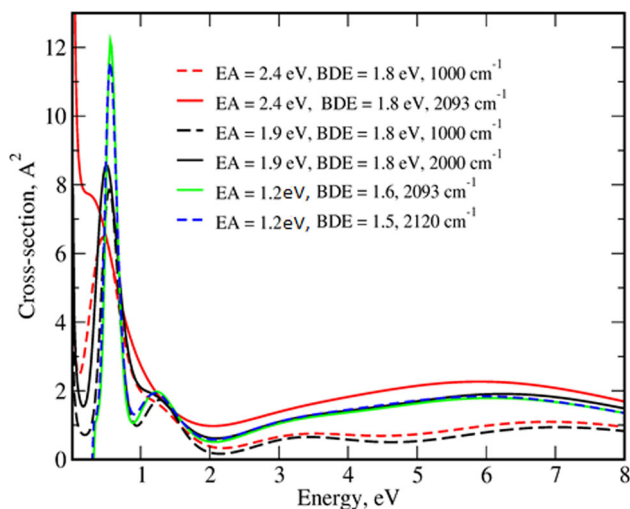


**Fig. 9** Dissociative electron attachment cross section of  $\text{Fe}(\text{CO})_5$  as a function of electron affinity (EA), bond dissociation energy (BDE), and vibrational frequency (for 0.2 eV incident electron energy)

band or to the 1 eV wide  $\text{Fe}(\text{CO})_4^-$  shoulder starting at 0.8 eV. The CO-stretch for 0.7 eV band has been reported in the literature to be due to the same  $\pi^*$  resonance as the 1.3 eV band, as Feshbach resonances are usually 0–0.4 eV lower than the parent electronically excited state. Our calculations took into account an electron affinity of 1.2–2.4 eV and a vibrational frequency in the range 1000–2100  $\text{cm}^{-1}$  with a user-defined basis set based on cc-pVDZ with  $\text{C}_{2v}$  geometry.

The resonances were found with the R-matrix routine RESON [29]. RESON returns all the resonances found in the process for each energy range. We calculate DEA cross sections using specific dissociation energy, electron affinity and the effective mass corresponding to the fragmentation channel.

The total cross sections calculated from the DEA process are presented in Fig. 9. While the positions of the peaks are generally determined by the positions of the resonances and not by the parameters of the DEA model, they may slightly shift or get wider, and the relative heights also change as a function of the electron affinity, bond dissociation energy, and the vibrational frequency (to a lesser extent) which are, in turn, functions of the fragmentation channel. The main changes can be observed at low energies. Red curves in Fig. 9 correspond to the electron affinity and the dissociation energy leading to the formation of  $\text{Fe}(\text{CO})_4^-$ . For comparison, we show the cross section for two vibrational frequencies: 1000  $\text{cm}^{-1}$  and 2000  $\text{cm}^{-1}$ . One can see that the peak at 0 becomes more prominent if the vibrational frequency is lower. These curves describe DEA below 1 eV.

The black curves correspond to the second fragmentation channel and the formation of  $\text{Fe}(\text{CO})_3^-$ . The relevant energy region is 1–2.5 eV, and for this level, the lower vibrational frequencies lead to the prevalence of the peaks at lower energies. Comparing the red and the

black sets of curves, one can see lower electron affinity leads to a more pronounced peak (or better-separated peaks).

At higher energies and for the parameters corresponding to  $\text{Fe}(\text{CO})_2^-$  and  $\text{Fe}(\text{CO})^-$ , the specific peak structure cannot be resolved, although one can see the signatures of the resonances between 3 and 4 eV and 6 and 7 eV.

A peak at 0.6 eV with the highest intensity is observed in the range of  $12.5 \times 10^{-16} \text{ cm}^2$  corresponding to  $\text{Fe}(\text{CO})_4^-$ , followed by a second peak corresponding to  $\text{Fe}(\text{CO})_3^-$  around 1.4 eV with cross sections in the range of  $2.2 \times 10^{-16} \text{ cm}^2$  and a  $\text{Fe}(\text{CO})_2^-$  peak between 4 and 5 eV, the  $\text{Fe}^-$  and  $\text{FeCO}^-$  peaks are overlapping and further partial calculations are run separately for each of them. The estimation method for partial cross sections in the DEA process is not a replacement for experimental data and calculations, but a cross-check method.

## 6 Conclusions

In this paper, we report new results on DEA studies of the  $\text{Fe}(\text{CO})_5$  molecule using the velocity map imaging method and Quantemol-N simulations of the cross-section data. The experimental method of velocity map imaging offered valuable information through which the kinetic energies and angular distribution of the anions of  $\text{Fe}(\text{CO})_5$  were obtained in the gas-phase ranging in energy from 0.2 to 10 eV. The process of fragmentation is known to be dissociative electron attachment undergoing at low energies and being similar to the processes taking place at low energies induced by secondary and backscattered electrons in FEBID processes. The complete fragmentation of  $\text{Fe}(\text{CO})_5$  stripping off all carbonyl groups makes it a great candidate for FEBID deposition. We have also presented theoretical calculations of the elastic, excitation and DEA cross sections using the Quantemol-N program. With its 11 atoms,  $\text{Fe}(\text{CO})_5$  is one of the largest molecule studied using Quantemol-N, the software limitation being set at 17 atoms all together. The higher mass central Fe atom, a heavier atom, makes the calculations more complex than for gases with a higher R-matrix radius, involving the use of virtual orbitals and higher-order basis-sets. We hope this data may be used in further simulations of  $\text{Fe}(\text{CO})_5$  within a FEBID processing system.

**Acknowledgements** MP recognizes receipt of a Marie Curie Early Career Award from the ELENA ITN which received funding from the European Union's Horizon 2020 research and innovation program under the Marie Skłodowska-Curie grant agreement No 722149. The authors wish to acknowledge the collection of DEA ion spectra in collaboration with P. Papp and M. Danko at Comenius University, Slovakia (presented in Fig. 3).

**Data Availability Statement** This manuscript has no associated data or the data will not be deposited. [Authors' comment: The datasets generated and/or analyzed during the current study are available from the corresponding author on reasonable request.]

#### Declarations

**Conflict of interest** We have no conflicts of interest to disclose, all authors contributed equally to the writing of the present article.

**Open Access** This article is licensed under a Creative Commons Attribution 4.0 International License, which permits use, sharing, adaptation, distribution and reproduction in any medium or format, as long as you give appropriate credit to the original author(s) and the source, provide a link to the Creative Commons licence, and indicate if changes were made. The images or other third party material in this article are included in the article's Creative Commons licence, unless indicated otherwise in a credit line to the material. If material is not included in the article's Creative Commons licence and your intended use is not permitted by statutory regulation or exceeds the permitted use, you will need to obtain permission directly from the copyright holder. To view a copy of this licence, visit <http://creativecommons.org/licenses/by/4.0/>.

### Appendix I: Anion resonances of Fe(CO)<sub>5</sub>

See Table 4 .

### Appendix II: The XYZ atomic coordinates used in the calculation

See Table 5 .

**Table 5** Atomic coordinates of Fe(CO)<sub>5</sub>

Atom	X, Å	Y, Å	Z, Å
Fe	0	0	0
C	0	- 2.0402	0
C	0	0	1.8462
C	1.5989	0	- 0.9231
C	- 1.5989	0	- 0.9231
C	0	2.0402	0
O	0	- 3.1438	0
O	0	0	2.9619
O	2.5651	0	- 1.4810
O	- 2.5651	0	- 1.4810
O	0	3.1438	0

**Table 4** Fe(CO)<sub>5</sub> electron affinity (EA) and bond dissociation energy (BDE)

Ions	Shuman et al. EA	Shuman et al BDE	Engelking and Lineberger EA	Engelking and Lineberger Fe-C BDE	Chen et al EA	Anion resonances of Fe(CO) <sub>5</sub>
Fe(CO) <sub>4</sub> <sup>-</sup>	2.4 + / - 0.3	1.81	1.26 + / - 0.02	1.0 + / - 0.3	n/a	0.2/0.6/1.2
Fe(CO) <sub>3</sub> <sup>-</sup>	1.915 + / - 0.085	1.84	1.22 + / - 0.02	1.0 + / - 0.3	n/a	1.3/3.4
Fe(CO) <sub>2</sub> <sup>-</sup>	1.22 + / - 0.02	1.55	1.8 + / - 0.2	1.4 + / - 0.3	n/a	4.2
Fe(CO) <sup>-</sup>	1.157 + / - 0.005	1.46	2.4 + / - 0.3	0.2 + / - 0.4	n/a	5.8/8.9
Fe <sup>-</sup>	0.151 + / - 0.003	n/a	n/a	n/a	0.153	7.9

## References

- J.M. De Teresa, A. Fernandez-Pacheco, Present and future applications of magnetic nanostructures grown by FEBID. *Appl. Phys. A* **117**, 1645–1658 (2014)
- W.F. van Dorp, C.W. Hagen, A critical literature review of focused electron beam induced deposition. *J. Appl. Phys.* **104**, 081301 (2008)
- M. Gavanin, H.D. Wanzenboeck, D. Belic, M.M. Shawrav, A. Persson, K. Gunnarsson, P. Svedlindh, E. Bertagnolli, Magnetic force microscopy study of shape engineered FEBID iron nanostructures. *Phys. Status Solidi A* **211**(2), 368–374 (2014)
- M. Huth, F. Porрати, O.V. Dobrovolskiy, Focused electron beam induced deposition meets materials science. *Microelectron. Eng.* **185–186**(2018), 9–28 (2018)
- T. Lukaszcyk, M. Schirmer, H.P. Steinrück, H. Marbach, Electron-beam-induced deposition in ultrahigh vacuum: lithographic fabrication of clean iron nanostructures. *Small* **4**(6), 841–846 (2008)
- R.M. Thorman, R.T.P. Kumar, D.H. Fairbrother, Ingólfsson, The role of low-energy electrons in focused electron beam induced deposition: four case studies of representative precursors, *Beilstein. J. Nanotechnol.* **6**, 1904–1926 (2015)
- R. Kumar, I. Unlu, S. Barth, O. Ingólfsson, D.H. Fairbrother, Electron induced surface reactions of  $\text{HFeCo}_3(\text{CO})_{12}$ , a bimetallic precursor for focused electron beam induced deposition (FEBID). *J. Phys. Chem. C* **122**, 2648–2660 (2018)
- I. Unlu, J. Spencer, K.R. Johnson, R. Thorman, O. Ingólfsson, L. McElwee-White, D.H. Fairbrother, Electron induced surface reactions of  $(\eta^5\text{-C}_5\text{H}_5)\text{Fe}(\text{CO})_2\text{Mn}(\text{CO})_5$ , a potential heterobimetallic precursor for focused electron beam induced deposition (FEBID). *Phys. Chem. Chem. Phys.* **20**, 7862–7874 (2018)
- L. Sha, E. Porcel, H. Remita, S. Marco, M. Réfrégiers, M. Dutertre, F. Confalonieri, S. Lancombe, Platinum nanoparticles: an exquisite tool to overcome radioresistance. *Cancer Nanotechnol.* **8**(1), 4 (2017)
- A. Verkhovtsev, A. Traore, A. Muñoz, F. Blanco, G. García, Modeling secondary particle tracks generated by intermediate- and low-energy protons in water with the Low-Energy Particle Track Simulation code. *Radiat. Phys. Chem.* **130**, 371–378 (2017)
- N.S. Shuman, T.M. Miller, J.F. Friedman, A.A. Viggiano, Electron attachment to  $\text{Fe}(\text{CO})_n$  ( $n = 0–5$ ). *J. Phys. Chem. A* **2013**(117), 1102–1109 (2013)
- J. Lengyel, J. Fedor, M. Farnik, (2016) ligand stabilization and charge transfer in dissociative ionization of  $\text{Fe}(\text{CO})_5$  aggregates. *J. Phys. Chem. C* **120**, 17810–17816 (2016)
- K. Kunnus, I. Josefsson, I. Rajkovic, S. Schreck, W. Quevedo, M. Beye, C. Weniger, S. Grübel, M. Scholz, D. Nordlund, W. Zhang, R.W. Hartsock, K.J. Gaffney, W.F. Schlotter, J.J. Turner, B. Kennedy, F. Hennies, F.M.F. de Groot, S. Techert, M. Odelius, Ph. Wernet, A. Föhlich, Identification of the dominant photochemical pathways and mechanistic insights to the ultrafast ligand exchange of  $\text{Fe}(\text{CO})_5$  to  $\text{Fe}(\text{CO})_4\text{EtOH}$ . *Struct. Dyn.* **3**, 043204 (2016)
- P. Aiswaryalakshmi, D. Mani, E. Arunan, Fe as hydrogen/halogen bond acceptor in square pyramidal  $\text{Fe}(\text{CO})_5$ . *Inorg. Chem.* **52**, 9153–9161 (2013)
- P. Wernet, K. Kunnus, I. Josefsson, I. Rajkovic, W. Quevedo, M. Beye, S. Schreck, S. Grübel, M. Scholz, D. Nordlund, W. Zhang, R.W. Hartsock, W.F. Schlotter, J.J. Turner, B. Kennedy, F. Hennies, F.M.F. de Groot, K.J. Gaffney, S. Techert, M. Odelius, A. Föhlich, Orbital-specific mapping of the ligand exchange dynamics of  $\text{Fe}(\text{CO})_5$  in solution. *Nature* **520**, 78–81 (2015)
- J. Munro, S. Harrison, M. Fujimoto, J. Tennyson, A dissociative electron attachment cross-section estimator. *J Phys. Conf. Ser.* **388**, 012013 (2012)
- M. Allan, M. Lacko, P. Papp, Š Matejčík, M. Zlatař, I.I. Fabrikant, J. Kočíšek, J. Fedor, Dissociative electron attachment and electronic excitation in  $\text{Fe}(\text{CO})_5$ . *Phys. Chem. Chem. Phys.* **20**, 11692 (2018)
- J. Lengyel, P. Papp, Š Matejčík, J. Kočíšek, M. Fárník, J. Fedor, (2017), Suppression of low-energy dissociative electron attachment in  $\text{Fe}(\text{CO})_5$  upon clustering. *Beilstein J. Nanotechnol.* **8**, 2200–2207 (2017)
- P.C. Engelking, W.C. Lineberger, Laser photoelectron Spectrometry of the Negative Ions of Iron and Iron Carbonyls. Electron affinity determination for the series  $\text{Fe}(\text{CO})_n$   $n = 0, 1, 2, 3, 4$ . *J. Am. Chem. Soc.* **101**, 19 (1979)
- X. Chen, Z. Luo, J. Li, C. Ning, Accurate electron affinity of iron and fine structures of negative iron ions. *Sci. Rep.* **6**, 24996 (2016)
- M. Lacko, P. Papp, K. Wnorowski, Š Matejčík, Electron-induced ionization and dissociative ionization of iron pentacarbonyl molecules. *Eur. Phys. JD* **69**, 84 (2015)
- J. Lengyel, J. Kočíšek, J. Fedor, Self-scavenging of electrons in  $\text{Fe}(\text{CO})_5$  aggregates deposited on argon nanoparticles. *J Phys. Chem. C* **120**, 7397–7402 (2016)
- J.R. Hamilton, J. Tennyson, S. Huang, M.J. Kushner, Calculated cross sections for electron collisions with  $\text{NF}_3$ ,  $\text{NF}_2$  and  $\text{NF}$  with applications to remote plasma sources. *Plasma Sources Sci. Technol.* **26**, 065010 (2017)
- M.-Y. Song, J.-S. Yoon, H. Cho, G.P. Karwasz, V. Kokoouline, Y. Nakamura, J. Tennyson, Cross sections for electron collisions with methane. *J. Phys. Chem. Ref. Data* **44**(2), 023101 (2015)
- K. Norwood, A. Ali, G.D. Flesh, C.Y. Ng, A photoelectron-photoion coincidence study of  $\text{Fe}(\text{CO})_5$ . *J. Am. Chem. Soc.* **1990**(112), 7502 (1990)
- J. Clayden, N. Greeves, S. Warren, *ChemTube3D - Interactive 3D Organic Reaction Mechanisms*, <http://www.chemtube3d.com/>. Accessed November 2019, (2008)
- O. Rubner, V. Engel, M.R. Hachey, C. Daniel, A CASSCF/MR-CCI study of the excited states of  $\text{Fe}(\text{CO})_5$ . *Chem. Phys. Lett.* **302**(1999), 481–494 (1999)
- J. Tennyson, C.J. Noble, Reson - a program for the detection and fitting of breit-wigner resonances. *Comput. Phys. Commun.* **33**, 421–424 (1984)
- E. Szymańska, V.S. Prabhudesai, N.J. Mason, E. Krishnakumar, (2013) Dissociative electron attachment to acetaldehyde,  $\text{CH}_3\text{CHO}$  A laboratory study using the velocity map imaging technique. *Phys. Chem. Chem. Phys.* **15**, 998–1005 (2013)

30. J. Lengyel, P. Papp, S. Matejčík, J. Kočíšek, J. Fedor, M. Farnik, Suppression of low-energy dissociative electron attachment in Fe(CO)<sub>5</sub> upon clustering. *Beilstein J. Nanotechnol.* **8**, 2200–2207 (2017)
31. S.A. Trushin, W. Fuss, K.L. Kompa, W.E. Schmid, (2000) femtosecond dynamics of Fe(CO)<sub>5</sub> photodissociation at 267 nm studied by transient ionization. *J. Phys. Chem. A* **104**, 1997–2006 (2000)
32. S. Massey, A.D. Albas, L. Sanche, Role of Low-Energy Electrons (< 35 eV) in the Degradation of Fe(CO)<sub>5</sub> for Focused Electron Beam Induced Deposition Applications: Study by Electron Stimulated Desorption of Negative and Positive Ions. *J. Phys. Chem. C* **119**, 12708–12719 (2015)
33. Willock D. (2009) *Molecular Symmetry*. Wiley, p. 127
34. Sathyanarayana N. (2004) *Vibrational Spectroscopy: Theory and Applications*. New Age International, p. 368
35. R.R. Squires, D. Wang, L.S. Sunderlin, Metal carbonyl bond strengths in Fe(CO)<sub>n</sub><sup>-</sup> and Ni(CO)<sub>n</sub><sup>-</sup>. *J. Am. Chem. Soc.* **114**, 2788–2796 (1992)
36. P.T. Snee, C.K. Payne, S.D. Mebane, K.T. Kotz, C.B. Harris, Dynamics of photosubstitution reactions of Fe(CO)<sub>5</sub>: an ultrafast infrared study of high spin reactivity. *J. Am. Chem. Soc.* **123**(28), 6909–6915 (2001)
37. M. Besora, J.-L. Carreón-Macedo, A.J. Cowan, M.W. George, J.N. Harvey, P. Portius, K.L. Ronayne, X.-Z. Sun, M. Towrie, A combined theoretical and experimental study on the role of spin states in the chemistry of Fe(CO)<sub>5</sub> photoproducts. *J. Am. Chem. Soc.* **131**, 3583–3592 (2009)
38. C. Daniel, M. Benard, A. Dedieu, R. Wiest, A. Veillard, Theoretical aspects of the photochemistry of organometallics. 3. Potential energy curves for the photodissociation of Fe(CO)<sub>5</sub>. *J. Phys. Chem.* **88**(21), 4805–4811 (1984)
39. D. Nandi, V.S. Prabhudesai, E. Krishnakumar, Velocity slice imaging for dissociative electron attachment. *Rev. Sci. Instrum.* **76**, 053107 (2005)
40. W.J. Brigg, J. Tennyson, M. Plummer, R-matrix calculations of low-energy electron collisions with methane. *J. Phys. B At. Mol. Opt. Phys.* **47**, 185203 (2014)
41. B. Goswami, R. Naghma, B. Antony, Electron scattering from germanium tetrafluoride. *RSC Adv.* **4**, 63817 (2014)
42. D.R. Sieglaff, R. Rejoub, B.G. Lindsay, R.F. Stebbings, Absolute partial cross sections for electron-impact ionization of CF<sub>4</sub> from threshold to 1000eV. *J. Phys. B At. Mol. Opt. Phys.* **34**, 1289–1297 (2001)
43. R.N. Bhargava, V.S. Prabhudesai, E. Krishnakumar, Dynamics of the dissociative electron attachment in H<sub>2</sub>O and D<sub>2</sub>O: The A1 resonance and axial recoil approximation. *J. Chem. Sci.* **124**(1), 271–279 (2012)
44. R.N. Bhargava, E. Krishnakumar, Dissociative electron attachment resonances in ammonia: a velocity slice imaging based study. *J. Chem. Phys.* **136**, 164308 (2012)
45. B. Ram, E. Krishnakumar, Dissociative electron attachment to methane probed using velocity slice imaging. *Chem. Phys. Lett.* **511**(2011), 22–27 (2011)
46. K. Gope, V. Tadsare, V.S. Prabhudesai, N.J. Mason, E. Krishnakumar, (2016) Negative ion resonances in carbon monoxide. *Eur. Phys. JD* **70**, 134 (2016)
47. E. Bjarnason, B. Omarsson, S. Engmann, F.H. Omarsson, O. Ingólfsson, Dissociative electron attachment to titanium tetrachloride and titanium tetraisopropoxide. *Eur. Phys. JD* **68**, 101 (2014)